Simulation and Planning of a Magnetically Actuated Microrobot Navigating in the Arteries

Karim Belharet, David Folio, *Member, IEEE,* and Antoine Ferreira, *Member, IEEE*

***Abstract*—This work presents a preoperative microrobotic surgical simulation and planning application. The main contribution is to support computer-aided minimally invasive surgery (MIS) procedure using untethered microrobots that have to navigate within the arterial networks. We first propose a fast interactive application (with endovascular tissues) able to simulate the blood flow and microrobot interaction. Secondly, we also propose a microrobotic surgical planning framework, based on the anisotropic Fast Marching Method (FMM), that provides a feasible pathway robust to biomedical navigation constraints. We demonstrate the framework performance in a case study of the treatment of peripheral arterial diseases (PAD).**

***Index Terms*—Microrobotics, minimally invasive surgery, blood flow simulation, anisotropic path planning.**

I. Introduction

PREOPERATIVE surgical simulation and planning is a critical stage in medical decision-making and in the design of novel microrobotic minimally invasive surgery (MIS) techniques [1,2]. Due to the lack of anatomic consistency, preoperative planning with virtual and physical models of the system could improve the chances of achieving predictable intraoperative results. To this aim, it is mandatory to cope with potential conflicts between the intervention purposes of the microrobotic surgical system and the biological laws governing the patient body. To improve microrobotic MIS procedure significant progress has been made in three dimensional (3D) imagers [3]; modeling software for anatomy and vascular networks representation [4]; and biomechanical modeling of interactions between tissues and MIS tools. These advances have been mainly developed for catheter or guidewire-based operations [5,6], or gastrointestinal endoscopic capsules [7,8]. In contrast, there has been fewer works in the area of untethered microrobots for cardiovascular interventions [1,9]. To date, even in the case of a successfully performed procedure, the choice of a microrobot's design (shape, size, materials, locomotion abilities…) plays a key role. Indeed, these factors affect the microrobot propulsion that depends mainly on the motile, fluidic and friction forces between the endovascular device and the vessel. Therefore, the development of training applications or interactive planning systems, where the robotician or physician is able to design different microrobots and then test their behaviors in a patient-specific context, will be very helpful. A few applications focusing on interventional MIS have been developed or commercialized [10,11] until now. These applications include interactive models of catheters [5], endoscopic capsules [7], but do not address the challenging topic of modeling untethered microrobots [12] and their complex interactions with the blood flow and vessels walls [1]. Most proposed solutions use finite element modeling (FEM)-based representations, or computational fluid dynamics (CFD) simulations. Such approaches are suitable when accurate modeling or simulation are a primary concern. However, they usually rely on commercial software (such as Fluents or Comsol), and the computation time (usually in hours) is incompatible with interactive simulation or clinical practice. Moreover, planning a reliable and feasible path against the blood flow and vessel networks constraints is an important issue to be addressed for innovative microrobot-aided MIS applications. For instance, S. Martel et al. propose to use potential fields and the breadth-first search algorithm to find a pre-planned path [13] which are then delimited by waypoints [9]. A first drawback in such discrete graph-search algorithms is that they suffer from metrication errors [14]. Moreover, it is difficult to cope explicitly with the anisotropy. Finally, most untethered microrobot propulsion schemes based on magnetic pulling have to face important constraints related to coils technology. The planned path has to reduce the maximum pulling gradients being applied to the coils, the operation time and to maintain the rising temperature of the coils within operating limits. It actually impacts different endovascular magnetic actuation systems based on Magnetic Resonance Navigation (MRN) [9], or Octomag system [15]. Thus, the planned pathway must satisfy these considerations to be reliable.

This work aims to propose a preoperative microrobotic surgical planning application with blood flow simulation that may use patient-specific data. In particular, the computer-aided optimization of the untethered microrobots for innovative MIS procedure is the main focus of our work. First, in Section II, after introducing the system model used by the microrobotic surgical simulation, we present the surgical planning framework. The proposed framework is based on the Fast Marching Method (FMM) [16]. In our previous work [17,18], the classical FMM with isotropic cost function has been proposed to extract the vessel centerline path. This first solution is suitable mainly to navigate far away from the vessel wall. However, as navigation in real vascular networks is directionally constrained by the biological environment, a new framework based on the *anisotropic* FMM [19] is proposed in this paper. Furthermore, the proposed method allows a multi-parameter optimization of the navigation path that takes into account: i) the technology of the magnetic system; ii) the microrobot design; and iii) the physiology of the patient. Finally, our approach ensures a smooth conveyance of the microrobot to destination robust to cardiovascular navigation

The authors are with Laboratoire PRISME, ENSI de Bourges, 88 boulevard Lahitolle, 18020 Bourges, France.
E-mail: firstname.name@ensi-bourges.fr

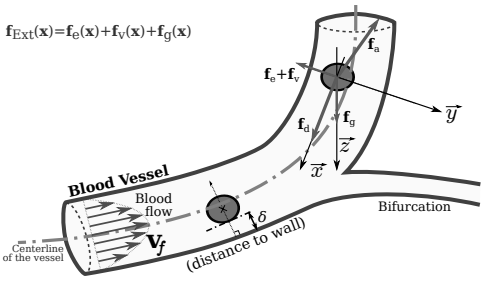

Fig. 1. Modeling scheme example in case of bead pulled microrobot.

constraints while minimizing the energy expenditure, to reduce the gradient pulling and system overheating. Specifically, we aim to get a *feasible path* by finding the min-energy pathway (which is not necessarily the shortest). Section III briefly describes our developed microrobotic surgical simulation and planning application, before illustrating its performance. As an illustration, we consider the treatment of peripheral arterial diseases (PAD), such as artery narrowing (stenosis). For instance, one possible surgical application is to target atherosclerotic plaques in stenosed arteries. One of the most common strategies is angioplasty, occasionally with stent implantation. Despite the high success rate, these solutions are not satisfactory, as vessel damage, infection and restenosis can appear at a later stage. Otherwise, a surgical microrobot for such vascular applications offers some novel solutions [1]. Specifically, microrobotic intervention based on chemical, mechanical or mechano-chemical could be achieved to treat vascular obstructions [2]. Finally, we discuss some open issues, evaluate the computational efficiency, and outline some future extends in Section IV. This study is concluded in Section V.

II. Methods

A. A modeling overview

Different types of devices could be used for MIS interventions from catheter and guidewires, to wireless microcapsules or microcarriers [1]. In this framework, any kind of untethered microdevice (termed as *microrobot* throughout the text) that has to perform endovascular navigation within blood flow is considered. More precisely, we consider any microsystem that could be modeled as:

$$m\dot{\mathbf{v}} = \mathbf{f}_{\mathrm{a}}(\mathbf{a}) + \mathbf{f}_{\mathrm{d}}(\mathbf{v}) + \mathbf{f}_{\mathrm{Ext}}(\mathbf{x}) \tag{1}$$

where $\mathbf{v}$ is the velocity of the device; m its mass; $\mathbf{f}_{\mathrm{a}}(\mathbf{a})$ is the *controlled* force, that is related to the control action $\mathbf{a} \in \mathcal{A}$, with $\mathcal{A}$ the *admissible controls* set; $\mathbf{f}_{\mathrm{d}}(\mathbf{v})$ denotes the fluid flow hydrodynamic drag force; and $\mathbf{f}_{\mathrm{Ext}}(\mathbf{x})$ are all other external forces, as depicted Fig. 1. Different external forces could be added to the model (1), such as the weight ($\mathbf{f}_g$), electrostatic ($\mathbf{f}_{\mathrm{e}}$), van der Waals ($\mathbf{f}_{\mathrm{v}}$), contact or steric forces. The interested reader may refer to [20] for detailed formulation of microforces. Fig.2 illustrates the evolution of these microforces with varying microrobot radius r and wrt. its distance to vessel wall δ. In particular, Fig. 2(f) shows that close to the centerline of the vessel ($\delta = R$) the electrostatic

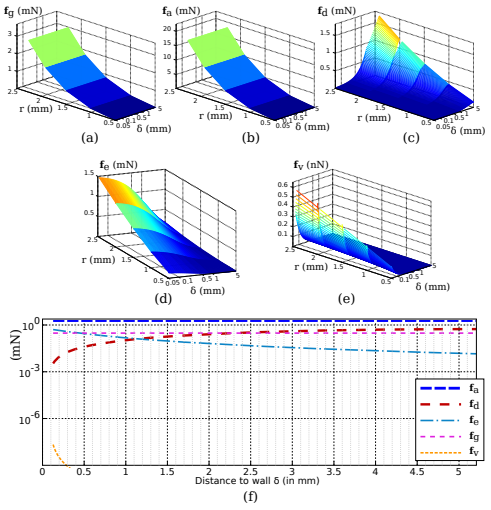

Fig. 2. Microforces evolution: (a) apparent weight $\mathbf{f}_g$ (b) magnetic force $\mathbf{f}_{\mathrm{a}}$ (with $\nabla B = 200\,\mathrm{mT/m}$), (c) drag force $\mathbf{f}_{\mathrm{d}}$ (with $\|\overline{\mathbf{v}}_{\mathrm{f}}\| = 400\,\mathrm{mm/s}$), (d) electrostatic force $\mathbf{f}_{\mathrm{e}}$, (e) van der Waals force $\mathbf{f}_{\mathrm{v}}$, as function of the distance to the vessel wall δ in artery ($R = 5\,\mathrm{mm}$) and wrt. the microrobot radius r. (f) Microforces acting on a microrobot with $r = 1\,\mathrm{mm}$ wrt. the distance to the vessel wall δ in artery ($R = 5\,\mathrm{mm}$).

and the van der Waals microforces are negligible compared to the other relevant forces. In addition, if the microrobot is never in contact with the vessel wall, the contact force could be omitted. Finally, most of the time because of the size of the microsphere, the effect of Brownian motion is also neglected.

B. Navigation Planning in Flow

1) Minimal Path Planning: Classically, a navigation pathway could be defined as a curve $\mathcal{P}$ linking a starting point $\mathbf{x}_0$ to any point $\mathbf{x}$. In the general case, a curve is a *minimal path*, also called a *geodesic*, wrt. the metric ϖ, if it globally minimizes the energy functional:

$$\mathcal{E}_{\varpi}(\mathcal{P}) = \int_{\mathcal{P}} \varpi(\mathcal{P}(l), \dot{\mathcal{P}}(l))dl, \tag{2}$$

with l the arclength parameter. The solution to the minimum path finding problem (2) could be obtained through the computation of the distance map $\mathcal{U} : \mathcal{C} \mapsto \mathbb{R}^+$, defined as: $\mathcal{U}(\mathbf{x}) = \min_{\mathcal{P}} \mathcal{E}(\mathcal{P})$, for any $\mathcal{P}$ linking $\mathbf{x}$ to $\mathbf{x}_0$ in the domain $\mathcal{C} \subset \mathbb{R}^d$ (with $d = 2, 3, 4\ldots$). In this context, Sethian [16] has proposed the Fast Marching Method (FMM). Indeed, the FMM converges to a smooth solution in the **continuous domain** even when it is implemented on a sampled environment, contrary to discrete graph-search algorithms. Especially, in the isotropic case, the FMM satisfies the Eikonal equation:

$$\begin{cases} \|\nabla \mathcal{U}(\mathbf{x})\| &= w(\mathbf{x}), \qquad \forall \mathbf{x} \in \mathcal{C} \\ \mathcal{U}(\mathbf{x}_0) &= 0 \end{cases} \tag{3}$$

where the isotropic cost function $w : \mathbf{x} \in \mathcal{C} \mapsto w(\mathbf{x}) \in \mathbb{R}^+$ is the metric. As the map $\mathcal{U}$ has a single local minimum, the geodesic can be retrieved with a simple gradient descent on $\mathcal{U}$ from a targeted seed $\mathbf{x}_{\mathrm{g}}$ to $\mathbf{x}_0$. The FMM provides a continuous solution to the minimum path problem by employing upwind differences and a causality condition [16]. The key issue of

the FMM is then to get an appropriate metric $w(\mathbf{x})$ which drives the front expansion efficiently to find a geodesic $\mathcal{P}$. In previous works [17,18], we have proposed to design such a metric on spatial consideration:

$$w : \mathbf{x} \in \mathcal{C} \mapsto \texttt{Vesselness}(\mathbf{x}) \in \mathbb{R}^+ \tag{4}$$

where $\texttt{Vesselness}(\mathbf{x})$ is a vesselness enhancement function. A typical $\texttt{Vesselness}(\mathbf{x})$ function could be designed using a multi-scale analysis of the Hessian matrix, as proposed by Frangi [21] or Sato [22]. This approach then allows to find the vessel centerline geodesic $\mathcal{P}_c$, as the considered vesselness filter gives their maximal response in the vessel center. We have applied this procedure to different sets of data, in 2D [17] as well as in 3D [18].

As mentioned previously the contact, electrostatic and van der Waals microforces are negligible when the microrobot navigates close to the centerline $\mathcal{P}_c$ (cf. Fig. 2). $\mathcal{P}_c$ is then the best solution to navigate far away from the vessels wall. However, navigation in real vascular networks is constrained by the biological environment, and can strongly modify the system behavior, leading to incompleteness in real intra-operative applications.

2) Anisotropic Path Planning: Navigating in blood flow implies some directional constraints. When the path finding problem has some preferred directions of travel it becomes *anisotropic*, i.e. the solutions depend on the configuration and directional constraints. In [19], the authors noticed that the FMM could be applied to isotropic or anisotropic problems, and they provided a numerical scheme to solve static Hamilton-Jacobi equations of the form:

$$\begin{cases} \|\nabla \mathcal{U}(\mathbf{x})\| &= \varpi(\mathbf{x}, \frac{\nabla \mathcal{U}(\mathbf{x})}{\|\nabla \mathcal{U}(\mathbf{x})\|}), \quad \forall \mathbf{x} \in \mathcal{C} \\ \mathcal{U}(\mathbf{x}_0) &= 0 \end{cases} \tag{5}$$

where the anisotropy expansion is the result of the dependence of ϖ on $\nabla \mathcal{U}(\mathbf{x})$. Nevertheless, the computational complexity of the FMM in the anisotropic case is growing significantly with the amount of anisotropy. The literature provides different variants of the FMM to deal with anisotropy, such as using a recursive approach [23], or iterative schemes [24]. Furthermore, in [14] anisotropic cost functions have been also proposed. The proposed basic idea is to take advantage of the original FMM efficiency, and to model the anisotropy thanks to a vector $\mathbf{f}$ of a field of force $\mathcal{F}$, leading to the following anisotropic metric:

$$\varpi : (\mathbf{x}, \mathbf{f}) \in \mathcal{C} \times \mathcal{F} \mapsto \varpi(\mathbf{x}, \mathbf{f}) \in \mathbb{R}^+ \tag{6}$$

Such an anisotropic cost function leads to anisotropic front-propagation, and gives better geodesic than isotropic FMM. To embed the directional constraints $\mathbf{f}$ within such an anisotropic FMM different specific cost functions have been proposed mainly for autonomous underwater vehicles (AUVs) [14,25]. The drag and flow forces have a significant effect on the motion of the AUV, which is a common problem with our microrobot planning problem. However, the proposed solution mainly deals with either the *min*-distance or the *min*-time path finding problem, and not minimizing directly neither the dynamics nor the motion applied to the system. Moreover, most existing approaches classically simplify the problem by assuming constant vehicle speed, or only spatially varying flow fields without time variation. Such limitations can generate physically unfeasible paths. Especially, in the presence of strong flows, incompleteness or incorrectness issues are reported [25].

3) Minimum-feasible-energy Planning: Most microrobot propulsion schemes usually require a limitation of the power consumption, and have a maximum available power. Moreover, considering only either the *min*-time or *min*-distance problem usually leads to compute high motion forces, that is reach the goal as fast as possible. But in our context, high motion implies high drag forces, and then high motion force $\mathbf{f}_\text{a}$ (limited by the maximum available magnetic forces) to be able to reach the targeted area. To minimize the energy expenditure, a basic idea is to use a classical power functional expression, that is:

$$p(\mathbf{x}, \mathbf{a}) = \langle \mathbf{f}(\mathbf{x}, \mathbf{a}) \cdot \mathbf{v}(\mathbf{x}) \rangle \tag{7}$$

where $\langle \cdot \rangle$ is the inner product of $\mathbb{R}^d$; $\mathbf{v}$ is a velocity; and $\mathbf{f}(\mathbf{x}, \mathbf{a})$ is the applied resultant force that embeds the controlled action $\mathbf{a} \in \mathcal{A}$. Using the optimal control approach, we propose the following anisotropic cost function:

$$\varpi(\mathbf{x}, \mathbf{f}) = \max_{\mathbf{a} \in \mathcal{A}} \langle \mathbf{f}(\mathbf{x}, \mathbf{a}) \cdot \mathbf{v}(\mathbf{x}) \rangle \tag{8}$$

This anisotropic cost formulation, as in [14,25], naturally incites the device to move in the direction of the force $\mathbf{f}$. Especially, $\varpi(\mathbf{x}, \mathbf{f})$ will imply that the FMM propagation (5) follows the force field constraints, that is $\frac{\nabla \mathcal{U}(\mathbf{x})}{\|\nabla \mathcal{U}(\mathbf{x})\|} \propto \mathbf{f}$. Finally, this new anisotropic formulation (8) using optimal control aspects embeds the system motion wrt. a finite defined admissible control set $\mathcal{A}$. This ensures that the given geodesic $\mathcal{P}$ is *really feasible* by the system and minimizes energy expenditure. Indeed, the metric $\varpi(\mathbf{x}, \mathbf{f})$ allows to consider both the biological constraints and the microrobot capabilities.

III. Results

A. Simulation and Planning Tool

The proposed framework has been integrated in a dedicated interactive microrobot surgical simulation and planning application. This application, depicted on Fig. 3, is based on the Visualization Toolkit (VTK) [26], the Insight Segmentation and Registration Toolkit (ITK) [27], and the Qt Toolkit [28]. Through the user interface (Fig. 3(b)), the surgeon realizes the following operating mode iteratively:

a) *Specifications:* The surgeon provides different parameters in the software (in the left panel on Fig. 3(b)) related to: i) the physiology of the patient (blood flow and viscosity, vessel's size and topology); ii) the technology of the magnetic system (coil's slew rate, maximum magnetic gradients, power limitations); and iii) the microrobot design (size, density, magnetic saturation).

b) *Simulations:* The surgeon initiates the simulation and planning process wrt. the specification constraints.

c) *Data analysis:* The surgeon analyses the power functional mapping and force field wrt. microrobot specifications.

This iterative process is conducted until the preoperative planning of plaque removal specifications are satisfied. We

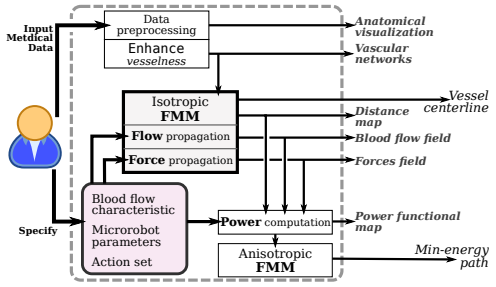

(a)

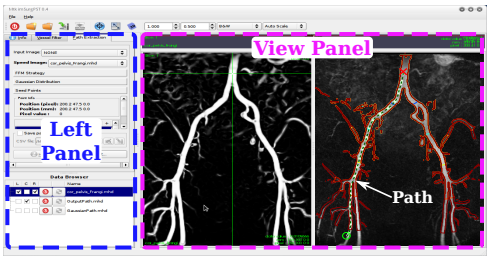

(b)

Fig. 3. Preoperative microrobot surgical simulation and planning application: (a) application workflow; (b) vessel centerline extraction example.

focus in the sequel on the main contributions of this paper that is the simulation and reliable vascular navigation planning.

B. Case study: peripheral arterial diseases

To assess the overall framework, we have performed a series of tests for both the microrobot within blood vessel model simulation and preoperative microrobotic MIS planning. We illustrate the proposed application for the treatment of peripheral arterial diseases (PAD). One possible application is to locate atherosclerotic plaque in stenosed arteries. In particular, stenosis implies an abnormal narrowing of the vessel which causes a decrease in blood flow. Different plaque removal tasks have already been realized by magnetically actuated microrobots navigating in occluded blood vessels [2]. In [29], shear-targeting of a thrombolytic drug in a mouse arterial thrombosis model using a microcarrier has been successfully tested. In [30], the rotation of the magnetic microrobot is at the origin of a drilling action through an occlusion in a vessel. In the following, we propose a preoperative planning of a magnetic microrobot navigating within the vasculature to the stenosed artery for plaque removal. We will consider here as case study the real Magnetic Resonance Angiogram (MRA) clinical dataset depicted on Fig. 4. As the proposed framework works in $\mathcal{C} \subset \mathbb{R}^d$ (with $d = 2, 3\ldots$), for the sake of clarity of the representation, we will only show here a Maximum Intensity Projection (MIP) image of the MRA. Here, the patient has a single level disease represented by an isolated stenosis in the iliac artery. As it is still a challenging issue to identify automatically the patient pathology and its location, the PAD is manually defined by the user.

C. Simulation Results

As previously mentioned, the simulation is based on a physics-based model (presented in details in [20]). When

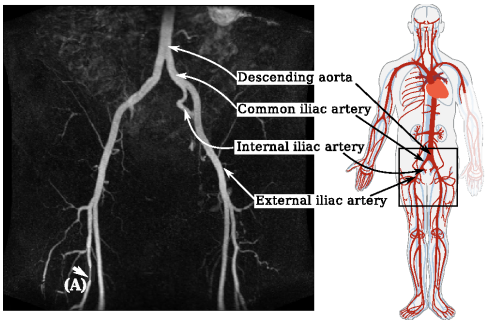

Fig. 4. Real MIP image from MRA (resolution of $N = 384 \times 384$ nodes) obtained in a patient with an isolated stenosis in the iliac artery (the white (A)-arrow), used to illustrate microrobotic MIS treatment simulation and planning.

interactive simulation is required (for training, intervention planning, etc.), a trade-off between computation time and accuracy has to be found. In our application, computational efficiency is more important than small-scale details, as we aim to increase the users interaction capabilities, whereas precision could be achieved using FEM or CFD simulation. To speed-up either the blood flow velocity or the force fields simulation computation, the basic FMM is extended to be able to compute these vector fields during the front propagation (see Fig. 3(a)). Indeed, using $\texttt{Vesselness}(\mathbf{x})$ isotropic cost function, the FMM front will extend only within the vascular structure. This allows to take advantage of the FMM efficiency, without using the whole dataset grids, and significantly reduce the overall computational time.

The blood flow velocity field simulation of the considered case study is illustrated on Fig.5. The interactive simulation tool takes into account that blood flow velocity intensity $\overline{\mathbf{v}}_\mathrm{f}$ on the vessel centerline decreases wrt. vessels radii, that is from about $\|\overline{\mathbf{v}}_\mathrm{f}^\mathrm{ad}\| \approx 400$ mm/s in descending aorta with a radius $R \approx 6.5$ mm, to $\|\overline{\mathbf{v}}_\mathrm{f}^\mathrm{ei}\| \approx 250$ mm/s in external iliac artery with a radius $R \approx 3.5$ mm. As one can see, the blood flow velocity field is modified in the considered stenosis case (narrowed vessel on Fig.5). The corresponding force field that will act on a neodymium microrobot with a radius $r = 500\ \mu$m is shown on Fig.6. In this simulation, only the weight $\mathbf{f}_g$ (in the $\overrightarrow{g}$-axis direction), drag $\mathbf{f}_\mathrm{d}$ and electrostatic $\mathbf{f}_\mathrm{e}$ forces are calculated. Let us notice that any force that can have an analytical expression and can be embedded in (1) can easily be added to the application. Finally, the realized interactive simulation application is also able to deal with periodic time-varying pulsatile blood flows, as presented on Fig. 7. The user defines the periodic pulsatile blood flow parameters [20], a number of time-steps, and can then browse the time-frame of either the blood flow velocity or the applied force field. Fig. 7(a) illustrates a typical periodic time-varying pulsatile blood flow that takes place in the descending aorta, and the row 7(b) describes the corresponding velocity field. Fig. 7(c) and 7(d) show the resulting force fields applied on the microrobot for two case studies, a microrobot of radius of $r = 250\,\mu$m and $r = 1.5$ mm, respectively. This demonstrates that when the microrobot's radius r or weight $\mathbf{f}_g$ increases, the resultant force becomes more important.

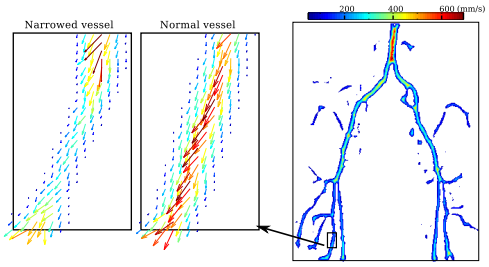

Fig. 5. Simulation results of the blood flow velocity field computation.

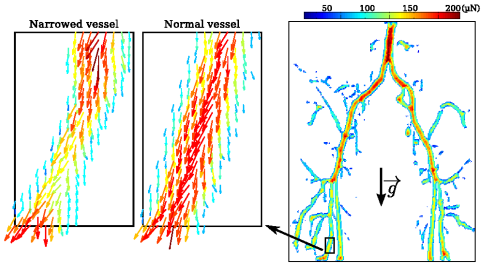

Fig. 6. Simulation results of the force field: $\mathbf{f} = \mathbf{f}_{\mathrm{d}}(\mathbf{v}) + \mathbf{f}_{\mathrm{e}}(\mathbf{x}) + \mathbf{f}_g$, applied on a microrobot of $r = 500$ μm radius.

D. Microrobotic surgical planning demonstration

Once the microrobot is specified (size, materials, etc.), the system's planning step only requires as user's input the starting $\mathbf{x}_0$ and ending points $\mathbf{x}_{\mathrm{g}}$. Next, to deal with the anisotropy of the media, the blood flow and force fields simulation results are used to compute the power functional map (7). The key issue is then to generate the controlled force field $\mathbf{f}_{\mathrm{a}}(\mathbf{a}), \forall \mathbf{a} \in \mathcal{A}$. First, the action magnitude has to be defined wrt. available actuation command. The action magnitude is usually the controlled magnetic gradient ($\mathbf{a} = \nabla B$), which implies the following magnetic force on a spherical device:

$$\mathbf{f}_{\mathrm{a}}(\nabla B) = D\tau_m \frac{4}{3}\pi r^3 \left(\mathbf{M}.\nabla\right)\nabla B, \tag{9}$$

where r is the microsphere radius; $\tau_m \in [0;1]$ is the volume ratio of the magnetic material; $\mathbf{M}$ its magnetization; and $D \in [0;1]$ is the duty-cycle, i.e., the ratio between the duration of the applied magnetic gradient for propulsion to the total period T.

The magnetic gradient used to propel a magnetic microrobot is assumed to be generated from various medical magnetic steering systems: ElectroMagnetic based Actuation (EMA) systems such as the Magnetic Catheter Steering System (a larger version of the Octomag system [15]) or the one developed in [30]; and Magnetic Resonance Navigation (MRN). The EMA systems are capable of generating maximum magnetic gradient fields up to $\mathbf{a}_{\max} = 350$ mT/m in closed-loop navigation control. In this case, the duty cycle is considered equal to $D = 1$ since the imaging modality is provided by either optical microscopy or X-ray imaging. These systems are more suitable for the navigation of millimeter-sized hard magnetic microrobots. The MRN system is based on clinical MRI systems, without any hardware upgrades. Such magnetic systems are usually limited to maximum values to $\mathbf{a}_{\max} = 80$ mT/m in closed-loop navigation control. Generally, the duty cycle is $D < 1$, since MR-imaging sequences and MR-tracking are provided by the same scanner to gather feedback positional information during MRN [9]. The MRN approach is more suitable for micrometer-sized soft magnetic microrobots. However, it should be noticed that experimental results have shown that therapeutic particles (known as TMMC), 50-60 μm diameter were navigated in arteries (rabbit models) and that MRN was done with gradient coils (capable of 450 mT/m with inner diameter suitable for limbs or head interventions) installed in the tunnel of clinical MRI scanners [31].

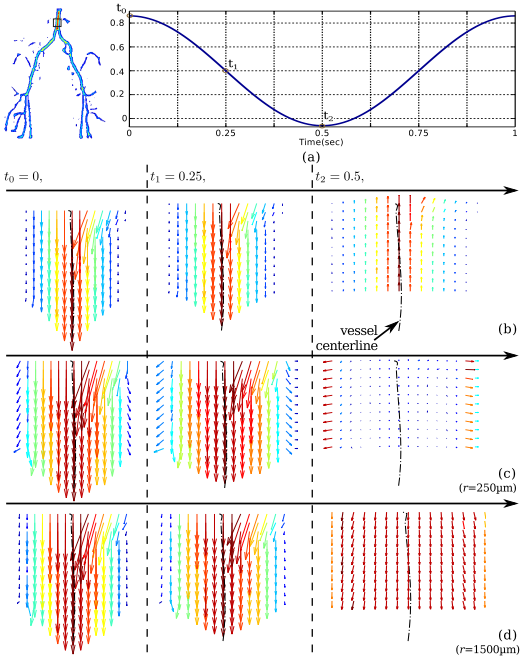

Fig. 7. Pulsatile blood flow simulation: (a) the periodic time-varying velocity in the descending aorta; (b) zoomed view of the blood flow velocity field; (c-d) zoomed view of the force field $\mathbf{f} = \mathbf{f}_{\mathrm{d}} + \mathbf{f}_{\mathrm{e}} + \mathbf{f}_g$ acting on a microrobot of: (c) $r = 250\,\mu$m, and (d) $r = 1500\,\mu$m for different time instants.

Our proposed FMM strategy can be adapted to each specific case by taking into account the duty-cycle D, the slew rate of the magnetic coils, and the maximum temperature coils. Secondly, the action direction should be defined. To this aim, we used some a priori knowledge about the goal direction, defined between $\mathbf{x}_0$ and $\mathbf{x}_{\mathrm{g}}$, provided by the isotropic FMM using $\texttt{Vesselness}(\mathbf{x})$ cost function (see Fig. 3(a)). Indeed, this FMM step provides the distance map $\mathcal{U}_c$ between $\mathbf{x}_0$ and $\mathbf{x}_{\mathrm{g}}$ (or reciprocally), and then the goal direction field $\nabla\mathcal{U}_c(\mathbf{x})$. This helps to define the appropriate *guidance field* $G(\mathbf{x}) \propto \nabla\mathcal{U}_c(\mathbf{x})$. Some variations could be added on the goal direction field to enlarge the guidance field set. The admissible control set $\mathcal{A}$ can then be defined as:

$$\mathcal{A} = \{\mathbf{A} \times \mathbf{G}\}, \tag{10}$$

where $\mathbf{A} \subset]0; \mathbf{a}_{\max}]$ is a finite set of action magnitudes, and $\mathbf{G} = \{G(\mathbf{x}) \sim [0; \frac{\pi}{2}]\}$ is the guidance field set. Let us recall that $\mathcal{A}$ could be filtered to consider some technological constraints (such as the duty-cycle, or the magnetic slew rate).

This planning framework has been validated on the case study dataset considering different microrobot sizes navigating within arteries. First, Fig. 8 demonstrates the influence of the

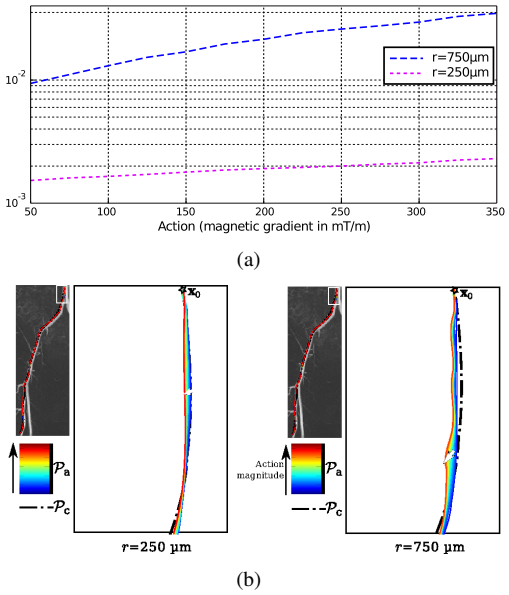

Fig. 8. Planning results on varying control action influence for a neodymium microrobot of size 250 μm and 750 μm: (a) the energy functional $\mathcal{E}_{\varpi}(\mathcal{P})$ wrt. the action magnitude (i.e. the magnetic gradient) and (b) zoomed view of the corresponding geodesics: $\mathcal{P}_c$ the vessel centerline and $\mathcal{P}_a$ the min-energy path for the varying action magnitude.

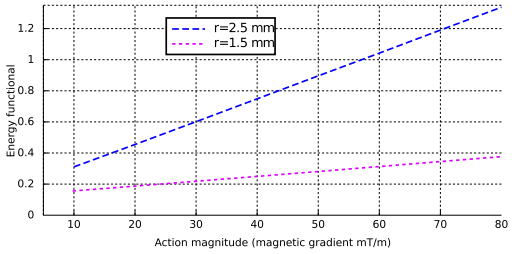

Fig. 9. Planning results on varying control action influence for a neodymium microrobot of size 1.5 mm and 2.5 mm in clinical MRI context.

motion force magnitude on finding the minimum-feasible-energy path. We noticed that as the motion force magnitude increased, the required energy $\mathcal{E}_{\varpi}(\mathcal{P})$ increased exponentially. This is significant for important microrobot size ($r = 750$ μm on Fig. 8(a)). Indeed, Fig. 8(b) shows that with much power the microrobot is more able to leave the vessel's centerline $\mathcal{P}_c$ (provided by the isotropic FMM) to reach the goal faster. If limited magnetic gradient magnitudes are available to propel the microrobot, such as in clinical MRI, Fig. 9 shows that increasing its size should overcome the power limitation. Therefore, the proposed *min*-energy path planning has been evaluated for various microrobot sizes and for EMA and MRN systems, as reported on Fig. 10. We can notice that for a microrobot radius bigger than 1.5 mm the curve length increases slightly, and starts to decrease significantly below 1 mm (cf. Fig. 10(a)). Furthermore, Fig. 10(b) depicts that the energy functional decreases significantly with the microrobot radius. In fact, the action force $\mathbf{f}_{\mathrm{a}}(\mathbf{a})$ decreases following a cubic power (L^3), minimizing the power budget. Therefore, it is more difficult for neodymium microrobots with a size below 750 μm to overcome the blood flow constraints that take place in the artery. Finally, as an illustration of the blood flow

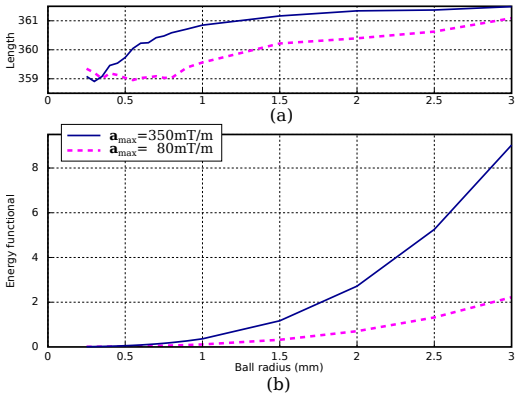

Fig. 10. Planning results with varying microrobot radii, for an EMA system ($\mathbf{a}_{\max} = 350\,\mathrm{mT/m}$) and a MRN ($\mathbf{a}_{\max} = 80\,\mathrm{mT/m}$): (a) the geodesic curvature length (in mm); and (b) the energy functional.

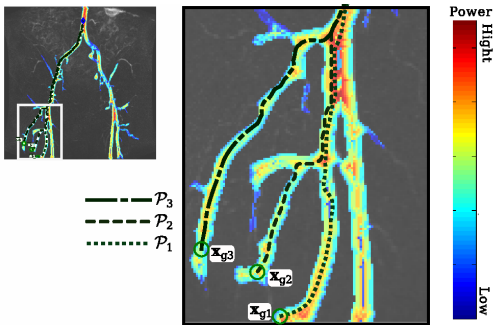

Fig. 11. Planning results using the proposed anisotropic cost function for a neodymium microrobot with $r = 1.5$ mm: three targeted point are specified ($\mathbf{x}_{\mathrm{g}1}$, $\mathbf{x}_{\mathrm{g}2}$ and $\mathbf{x}_{\mathrm{g}3}$). The colored map depicted the power functional level.

TABLE I
PLANNING RESULTS OF MINIMUM-FEASIBLE-PATH FOR THREE TARGETED POINT ($\mathbf{x}_{\mathrm{g}1}$, $\mathbf{x}_{\mathrm{g}2}$ AND $\mathbf{x}_{\mathrm{g}3}$) DEPICTED ON FIG.11

Geodesic #	Length (mm)	Energy $\mathcal{E}_{\varpi}(\mathcal{P})$
$\mathcal{P}_1$	360.086	0.6765
$\mathcal{P}_2$	**359.612**	0.5118
$\mathcal{P}_3$	361.735	**0.4879**

influence, Fig. 11 shows the planning results of our minimum-feasible-path finder for three targeted points ($\mathbf{x}_{\mathrm{g}1}$, $\mathbf{x}_{\mathrm{g}2}$ and $\mathbf{x}_{\mathrm{g}3}$), and Table I lists the curve lengths of their geodesic ($\mathcal{P}_1$, $\mathcal{P}_2$ and $\mathcal{P}_3$) and the energy functional $\mathcal{E}_{\varpi}(\mathcal{P})$. The *min*-energy geodesic is curve $\mathcal{P}_3$, while the shortest length is $\mathcal{P}_2$. This means that although $\mathcal{P}_3$ is longer than $\mathcal{P}_2$, $\mathcal{P}_3$ consumes less energy.

IV. DISCUSSION

The most computationally intensive part of the microrobotic surgical application is the vesselness filter (that provides $\mathtt{Vesselness}(\mathbf{x})$ cost function) based on a multiscale analysis of the Hessian matrix [21]. This multiscale interpretation of eigenvalues of the Hessian matrix could be improved thanks to parallelization through GPU implementation. Furthermore, as mentioned, instead of using the overall dataset grid (in the case study $N = 147\,456$), the vector fields simulations are performed on only 18 941 nodes corresponding to the vasculature. Thus, on an Intel Core2 3Ghz processor, one simulation time

takes less than 150 ms. For the periodic pulsatile blood flow, this allows to compute one cardiac cycle with 50 time-steps in less than 8 s. Therefore, the combination of the microrobot and the caradiovascular model together with the FMM may become accurate enough to support interactive microrobotic surgical planning applications. Finally, in the planning step, the main computational aspect remains on action set $\mathcal{A}$ generation. This set $\mathcal{A}$ is related to the dimension of the action magnitude set $\mathbf{A}$ and guidance field set $\mathbf{G}$, specified by the users. For the case study with $\dim \mathcal{A} = \{10 \times 10\}$, the overall planning procedure needs a calculation time of about 36 s. This computational efficiency ensures a high level of interactivity for preoperative simulation, planning and navigation.

In the simulation process we have chosen to focus on computational efficiency, rather than on accurate blood flow simulations. Nonetheless, the vasculature and blood flow modeling are still strongly investigated by the communities, and remain an open issue. In future extends, we will use some analytical modeling of vessel bifurcation as in [20], to improve the blood flow simulation accuracy. Although the visualization of vector fields is still a challenging issue (especially in 3D), more intuitive flow rendering (such as streamline, streamribbon, etc.) could also be helpful for the microrobotic surgery applications.

V. Conclusion

In this study, a microrobotic surgical simulation and planning has been presented for the treatment of peripheral arterial diseases. However, the proposed framework could also be applied to other regions of the body, different therapy and various MIS microrobots. Especially, the results shows that interactive applications can be helpful to design the suitable microrobot design (e.g. shape, size, materials, etc.) wrt. anatomic consistency to improve microrobotic surgical applications. Hence, preoperative surgical planning with blood flow simulation provides useful information for understanding cardiovascular pathologies, predicting their onset and choosing an optimal therapy strategy for innovative microrobotic MIS procedure.

Acknowledgment

The PhD student K. Belharet is supported by the Nano-IRM project, founded by Region Centre and City of Bourges.

References

[1] B. J. Nelson, I. K. Kaliakatsos, and J. J. Abbott, "Microrobots for minimally invasive medicine," *Annual Review of Bio.med. Eng.*, vol. 12, no. 1, pp. 55–85, 2010.

[2] P. Miloro, E. Sinibaldi, A. Menciassi, and P. Dario, "Removing vascular obstructions: a challenge, yet an opportunity for interventional microdevices," *Bio.med. Microdevices*, vol. 14, pp. 511–532, 2012.

[3] R. M. Satava, "Virtual reality, telesurgery, and the new world order of medicine," *Computer Aided Surgery*, vol. 1, no. 1, pp. 12–16, 1995.

[4] K. Sun, Z. Chen, and S. Jiang, "Local morphology fitting active contour for automatic vascular segmentation," *IEEE Trans. Biomed. Eng.*, vol. 59, no. 2, pp. 464–473, Feb. 2012.

[5] Y. Ganji and F. Janabi-Sharifi, "Catheter kinematics for intracardiac navigation," *IEEE Trans. Biomed. Eng.*, vol. 56, no. 3, pp. 621–632, Mar. 2009.

[6] W. Tang, T. R. Wan, D. A. Gould, T. How, and N. W. John, "A stable and real-time nonlinear elastic approach to simulating guide-wire and catheter insertions based on cosserat rod," *IEEE Trans. Biomed. Eng.*, vol. PP, no. 99, p. 1, 2012.

[7] F. Carpi, N. Kastelein, M. Talcott, and C. Pappone, "Magnetically controllable gastrointestinal steering of video capsules," *IEEE Trans. Biomed. Eng.*, vol. 58, no. 2, pp. 231–234, Feb. 2011.

[8] G. Ciuti, M. Salerno, G. Lucarini, P. Valdastri, A. Arezzo, A. Menciassi, M. Morino, and P. Dario, "A comparative evaluation of control interfaces for a robotic-aided endoscopic capsule platform," *IEEE Trans. Robot.*, vol. 28, no. 2, pp. 534–538, Apr. 2012.

[9] S. Tamaz, A. Chanu, J.-B. Mathieu, R. Gourdeau, and S. Martel, "Real-time MRI-based control of a ferromagnetic core for endovascular navigation," *IEEE Trans. Biomed. Eng.*, vol. 55, no. 7, pp. 1854–1863, Jul. 2008.

[10] (2012) Stereotaxis Inc. [Online]. Available: http://www.stereotaxis.com

[11] (2012) Sensei(r) x robotic catheter system. Hansen Medical. [Online]. Available: http://www.hansenmedical.com

[12] C. Pawashe, S. Floyd, and M. Sitti, "Modeling and experimental characterization of an untethered magnetic micro-robot," *The Int. J. of Robot. Research*, vol. 28, no. 8, pp. 1077–1094, 2009.

[13] W. Sabra, M. Khouzam, and S. Martel, "Use of 3D potential field and an enhanced breadth-first search algorithms for the path planning of microdevices propelled in the cardiovascular system," in *IEEE Int. Conf. of the Eng. in Med. and Bio. Soc.*, Apr. 2005.

[14] C. Pêtrès, Y. Pailhas, P. Patron, Y. Petillot, J. Evans, and D. Lane, "Path planning for autonomous underwater vehicles," *IEEE Trans. Robot.*, vol. 23, no. 2, pp. 331–341, 2007.

[15] M. Kummer, J. J. Abbott, B. E. Kratochvil, R. Borer, A. Sengul, and B. J. Nelson, "Octomag: An electromagnetic system for 5-dof wireless micromanipulation," *IEEE Trans. Robot.*, vol. 26, no. 6, pp. 1006–1017, Sep. 2010.

[16] J. A. Sethian, *Level set methods and fast marching methods: evolving interfaces in computational geometry, fluid mechanics, computer vision, and materials science*. Cambridge University Press, 1999.

[17] K. Belharet, D. Folio, and A. Ferreira, "Endovascular navigation of a ferromagnetic microrobot using MRI-based predictive control," in *IEEE/RSJ Int. Conf. on Intel. Robots and Syst.*, Taiwan, Oct. 2010.

[18] ——, "3D MRI-based predictive control of a ferromagnetic microrobot navigating in blood vessels," in *IEEE RAS & EMBS Int. Conf. on BioMed. Robot. and BioMechatron.*, Tokyo, Japan, Sep. 2010.

[19] J. A. Sethian and A. Vladimirsky, "Ordered upwind methods for static hamilton-jacobi equations: theory and algorithms," *SIAM J. on Numerical Analysis*, vol. 41, no. 1, pp. 325–363, 2003.

[20] L. Arcèse, M. Fruchard, and A. Ferreira, "Endovascular Magnetically-Guided Robots: Navigation Modeling and Optimization," *IEEE Trans. Biomed. Eng.*, no. 99, pp. 1–12, Sep. 2011.

[21] A. Frangi, W. Niessen, K. Vincken, and M. Viergever, "Multiscale vessel enhancement filtering," *Lect. Notes in Comp. Scie.*, pp. 130–137, 1998.

[22] Y. Sato, S. Nakajima, H. Atsumi, T. Koller, G. Gerig, S. Yoshida, and R. Kikinis, "Three-dimensional multi-scale line filter for segmentation and visualization of curvilinear structures in medical images," *Med. Imag. Anal.*, vol. 2, no. 2, pp. 143–168, 1998.

[23] E. Konukoglu, M. Sermesant, O. Clatz, J.-M. Peyrat, H. Delingette, and N. Ayache, "A recursive anisotropic fast marching approach to reaction diffusion equation: Application to tumor growth modeling," in *Inf. Processing in Med. Imag.*, N. Karssemeijer and B. Lelieveldt, Eds., vol. 4584. Springer, 2007, pp. 687–699.

[24] F. Bornemann and C. Rasch, "Finite-element discretization of static hamilton-jacobi equations based on a local variational principle," *Computing and Visualization in Science*, vol. 9, pp. 57–69, 2006.

[25] M. Soulignac, "Feasible and optimal path planning in strong current fields," *IEEE Trans. Robot.*, no. 99, pp. 1–10, Feb. 2011.

[26] (2012) The visualization toolkit (VTK). Kitware. [Online]. Available: http://www.vtk.org

[27] (2012) Insight segmentation and registration toolkit (ITK). Kitware. [Online]. Available: http://www.itk.org

[28] (2012) Qt-a cross-platform application and UI framework. Nokia. [Online]. Available: http://qt.nokia.com/

[29] N. Korin, M. Kanapathipillai, B. Matthews, M. Crescente, A. Brill, T. Mammoto, K. Ghosh, S. Jurek, S. Bencherif, D. Bhatta *et al.*, "Shear-activated nanotherapeutics for drug targeting to obstructed blood vessels," *Science*, vol. 337, no. 6095, pp. 738–742, 2012.

[30] C. Yu, J. Kim, H. Choi, J. Choi, S. Jeong, K. Cha, J. oh Park, and S. Park, "Novel electromagnetic actuation system for three-dimensional locomotion and drilling of intravascular microrobot," *Sensors and Actuators A: Physical*, vol. 161, no. 1-2, pp. 297–304, 2010.

[31] P. Pouponneau, J.-C. Leroux, G. Soulez, L. Gaboury, and S. Martel, "Co-encapsulation of magnetic nanoparticles and doxorubicin into biodegradable microcarriers for deep tissue targeting by vascular MRI navigation," *Biomaterials*, vol. 32, no. 13, pp. 3481–3486, 2011.